 doi: 10.1111/j.1365-246X.2008.03720.x

Surface wave tomography of the western United States from ambient seismic noise: Rayleigh and Love wave phase velocity maps

Fan-Chi Lin, Morgan P. Moschetti and Michael H. Ritzwoller

Center for Imaging the Earth's Interior, Department of Physics, University of Colorado at Boulder, Boulder, CO 80309-0390, *USA.*
E-mail: linf@colorado.edu

Accepted 2007 December 24. Received 2007 December 22; in original form 2007 May 9

SUMMARY

We present the results of Rayleigh wave and Love wave phase velocity tomography in the western United States using ambient seismic noise observed at over 250 broad-band stations from the EarthScope/USArray Transportable Array and regional networks. All available three-component time-series for the 12-month span between 2005 November 1 and 2006 October 31 have been cross-correlated to yield estimated empirical Rayleigh and Love wave Green's functions. The Love wave signals were observed with higher average signal-to-noise ratio (SNR) than Rayleigh wave signals and hence cannot be fully explained by the scattering of Rayleigh waves. Phase velocity dispersion curves for both Rayleigh and Love waves between 5 and 40 speriod were measured for each interstation path by applying frequency–time analysis. The average uncertainty and systematic bias of the measurements are estimated using a method based on analysing thousands of nearly linearly aligned station-triplets. We find that empirical Green's functions can be estimated accurately from the negative time derivative of the symmetric component ambient noise cross-correlation without explicit knowledge of the source distribution. The average traveltime uncertainty is less than 1 s at periods shorter than 24 s. We present Rayleigh and Love wave phase speed maps at periods of 8, 12, 16,and 20 s. The maps show clear correlations with major geological structures and qualitative agreement with previous results based on Rayleigh wave group speeds.

Key words: Interferometry; Surface waves and free oscillatons; Seismic tomography; Crustal structure; North America.

1 INTRODUCTION

Surface wave tomography using ambient seismic noise, also called ambient noise tomography (ANT), is becoming an increasingly well-established method to estimate short period (<20 s) and intermediate period (between 20 and 50 s) surface wave speeds on both regional (Sabra *et al.* 2005; Shapiro *et al.* 2005; Kang & Shin 2006; Yao *et al.* 2006; Lin *et al.* 2007; Moschetti *et al.* 2007) and continental (Bensen *et al.* 2008; Yang *et al.* 2007) scales. The applicability of the method at long periods (>50 s) is also now receiving more attention (e.g. Bensen *et al.* 2008; Yang *et al.* 2007). In these studies, Rayleigh wave Green's functions between station-pairs are estimated by cross-correlating long time-sequences of ambient noise recorded simultaneously at both stations. These studies have established that, within reasonable tolerances, the measurements are repeatable when performed in different seasons, the Green's functions agree with earthquake records, dispersion curves agree with those measured from earthquakes, and the resulting tomography maps cohere with known geological structures such as sedimentary basins and mountain ranges. Applied to regional array data, such as the EarthScope/USArray Transportable Array (TA), PASSCAL experiments, or the Virtual European Broadband Seismic Network, the resulting dispersion maps display higher resolution and are obtained to much shorter periods than those typically derived from teleseismic earthquakes. This holds out the prospect to infer considerably higher resolution information about the crust and uppermost mantle over extended regions.

To date, these studies have concentrated exclusively on Rayleigh waves and predominantly have used the estimated empirical Green's functions to obtain only measurements of group speed. Yao *et al.* (2006) was the first to use the empirical Green's functions to estimate the Rayleigh wave phase speed. The two principle purposes of this paper are, first, to investigate the extension of ambient noise tomography to Love waves and, second, to make phase measurements in the western United States. In so doing, we use data from the EarthScope/USArray TA combined with other regional networks in the western United States. From its inception until 2006 October 31, over 250 TA stations were deployed in this region and operated for various lengths of time (Fig. 1). Moschetti *et al.* (2007) have used these stations recently to obtain Rayleigh wave group velocity maps at periods from 8 to 40 s using ANT. We explicitly extend this study to phase velocity measurements and also show for the first time that Love wave dispersion also can be measured from ambient noise and used to produce tomographic maps.

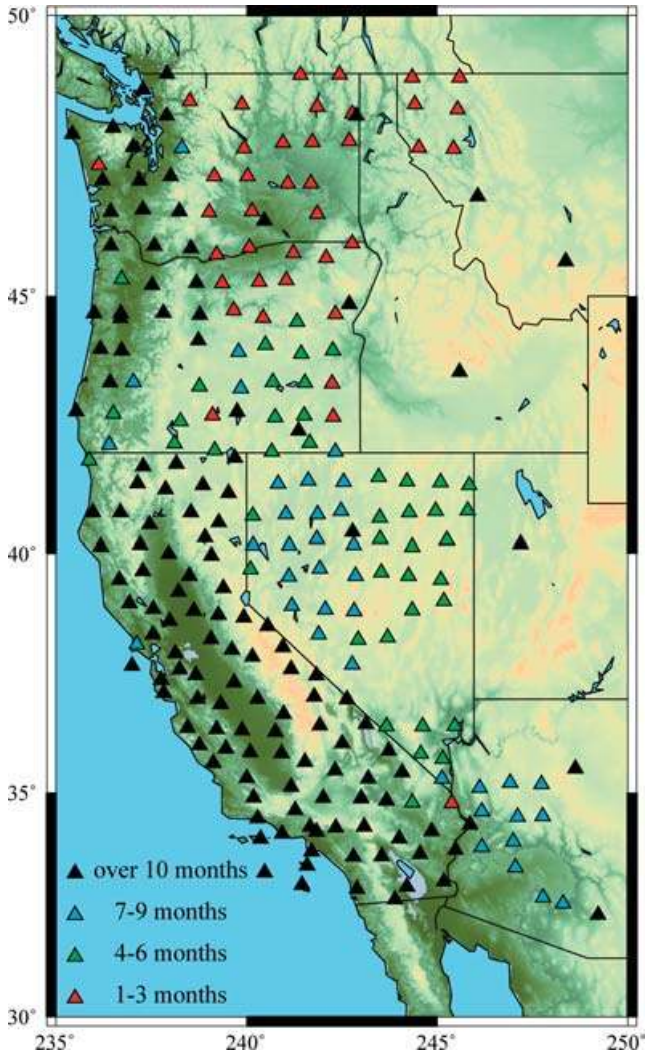

Figure 1. Location of the 253 broad-band stations used in this study, most from the Transportable Array component of USArray. The colour indicates the duration of the deployment during this study.

Although coda wave studies (Campillo & Paul 2003; Paul *et al.* 2005) demonstrated that Love wave signals could also be extracted from the diffusive wavefield, early ambient noise studies focused on Rayleigh waves at the expense of Love waves because of the higher locally generated noise on the horizontal components and general belief that the ambient noise source would be ineffective at directly generating Love waves. Numerous ambient noise source studies (e.g. Rhie & Romanowicz 2004, 2006; Stehly *et al.* 2006; Yang & Ritzwoller 2008) have concluded that coupling between ocean waves and the shallow seafloor produces long-range coherent noise on the vertical component. It has been believed, however, that it is more difficult to couple ocean waves with horizontal motions of the seafloor, which would make Love wave generation less efficient than that of Rayleigh waves. We show here that, in fact, Love waves appear clearly on the transverse–transverse cross-correlations between most station pairs, at least at periods shorter than 20 s.

The ability to make both Rayleigh and Love wave dispersion measurements at periods shorter than ∼20 s is important if radial anisotropy (the bifurcation of Vsv and Vsh) in the crust is to be observed. Shapiro *et al.* (2004) inferred strong radial anisotropy in the Tibetan crust, which they argued is caused by on-going crustal deformation. This inference is based on observing a discrepancy in the dispersion characteristics of Rayleigh and Love waves at periods for which the waves are sensitive to the crust. The thick crust of Tibet means that surface waves retain sensitivity to crustal structures to much longer periods than almost everywhere else in the world. For a crustal Rayleigh-Love discrepancy to be observed across the western United States, for example, where the average crustal thickness is less than half that of Tibet, Rayleigh and Love wave dispersion should be obtained to periods down to at least 10 s. Such periods are attenuated strongly from distant earthquakes and are largely unobservable, but are readily observed with ambient noise.

Past work also has concentrated on group rather than phase velocities for a number of reasons, perhaps most importantly because the 'initial phase' of ambient noise cross-correlation was not well understood and has been the subject of some speculation and confusion. Here we borrow the term 'initial phase' used in traditional earthquake analysis. Although the 'initial phase' here is purely caused by the inhomogeneity of the noise source distribution, it does share the same mathematic form and meaning in the context of describing the estimated Green's function, as we will show. Theoretical work done by Lobkis & Weaver (2001), Roux *et al.* (2005), Sabra *et al.* (2005) and Snieder (2004b) suggested that phase information in the surface wave Green's function can be recovered from the negative time derivative of the symmetric cross-correlation under the assumption of a spatially homogeneous ambient-noise source distribution. (The 'symmetric component cross-correlation' or 'symmetric signal' is the average of the cross-correlation at positive and negative correlation lag times.) Under this assumption, Yao *et al.* (2006) presented the first phase speed tomography based on ambient noise over southeast Tibet. However, how this assumption may alter, degrade or breakdown given the inhomogeneous distribution of ambient noise sources on earth has been unclear. The inhomogeneous distribution of noise sources is seen clearly by comparing the positive and negative lags of the cross-correlations (e.g. Lin *et al.* 2007). This type of observation is the basis for recent studies aimed at characterizing ambient noise sources (e.g. Stehly *et al.* 2006; Yang & Ritzwoller 2008). Yao *et al.* (2006) have also suggested that an inhomogeneous source distribution may account for part of the 1–3 per cent inconsistency they observed between phase velocity measurements made by the ambient noise method and the traditional earthquake-based two-station method between periods of 20–30 s.

Phase velocity measurements are desirable for the following reasons. First, as we show, the uncertainty of the phase velocity measurement is much smaller than that of the group velocity measurement. Second, within the same period band, phase velocity has a deeper sensitivity kernel and, therefore, constrains deeper velocity structures. Third, the dispersion relation for group velocity can be calculated from the dispersion relation for phase velocity, but the converse is not true.

In this paper, we address whether robust phase velocity measurements can be obtained from ambient noise without explicit knowledge of the source distribution. We use an empirical three-station method, discussed in Section 4.2, to test this hypothesis and also to identify systematic errors and the average uncertainty of real phase velocity measurements. Several previous studies have used the seasonal variability of the measurement to estimate their uncertainty (e.g. Bensen *et al.* 2007; Lin *et al.* 2007; Yang *et al.* 2007). Our method, however, avoids the possibility of repeated false measurements and systematic error. Synthetic cross-correlations based on different source distributions, discussed in Section 6.2, suggest that the 'initial phase' of the estimated Green's function would be approximately zero if the source distribution were to vary smoothly

over the constructive interference region. Combined with the result of the three-station method, we show that even though ambient noise sources have an inhomogeneous azimuthal distribution, ambient noise is distributed sufficiently homogeneously so that no additional phase shift is required in the estimated Green's function to account for irregularities in the source distribution.

We emphasize here that the only difference between ambient noise seismology and earthquake based seismology is the method used to obtain the waveforms used in the analysis. We extensively use terms borrowed from traditional earthquake seismology, such as 'initial phase', 'far field approximation' and 'signal-to-noise ratio' (SNR), to analyse and describe the estimated Green's function obtained by the cross-correlation of the ambient noise because these terms have the same meaning in this context.

The outline of this paper is as follows. We describe the method to obtain the estimated Green's functions for both Rayleigh and Love waves in Section 2. Evidence for the existence and retrievability of Love waves is presented in Section 3. In Section 4, we describe the method used to obtain the phase velocity measurements and the three-station method is developed to estimate the systematic errors and the average uncertainty of the measurements. Tomography maps at periods of 8, 12, 16 and 20 s for both Rayleigh and Love wave phase speeds are presented in Section 5. Throughout the paper, the straight ray theory is used and we focus on phase velocity measurements between periods of 8 and 24 s, where the highest SNRs are observed, on average.

2 DATA PROCESSING TO PRODUCE THE ESTIMATED GREEN'S FUNCTIONS

We analysed continuous data from over 250 broad-band stations in the western United States (Fig. 1) recorded between 2005 November 1 and 2006 October 31. Data from all three components (east, north, vertical) were used, and cross-correlations between all possible pairs of components from the two-stations were computed. The method to obtain the estimated Green's function is similar to that described for Rayleigh waves by Bensen *et al.* (2007). We summarize it briefly here with a concentration on the Love wave data processing.

All data are processed on a daily basis and then are stacked (superposed and added together) later. The mean, trend, and instrument response of the daily component (E, N, Z) seismograms are first removed and bandpass filtered between periods of 5 and 100 s. To speed up the process, we do not rotate the components into the radial (R) and transverse (T) directions for each station-pair until the component cross-correlations (E–E, E–N, N–N, N–E) are performed. Earthquake signals and instrumental irregularities are then removed by temporal normalization (Bensen *et al.* 2007). In order to postpone the component rotation until after cross-correlation, the east and north components are temporally normalized together. To achieve this, both components are first bandpass filtered between 15 and 50 s, a band that contains the most energetic surface wave signals from earthquakes. For each time point, the mean of the absolute value of each seismogram is computed in the 128 s window centred on that point. The values of the east and north components are compared, and the larger is used to define the inverse weight for that time point. That weight is then applied to both the north and east component time-series bandpassed between 5 and 100 s. This process effectively suppresses earthquake signals and is commutative with the rotation operator.

After temporal normalization, the signals are whitened in frequency. Before whitening, ambient noise is most energetic in the microseismic band below 20-s period. Frequency whitening is carried out to broaden the period band of the dispersion measurement. Again, to maintain the commutativity of the rotation operator, the east and north signals are whitened together. To do this, we first smooth the east amplitude spectrum by taking the average of the amplitude of spectrum with a 0.01 Hz moving window in the frequency domain. Because the spectra of both components are similar in shape, on average, we whiten both of them together simply by weighting the east and north signals in the frequency domain by the inverse of this smoothed east spectrum. In general, the phase dispersion measurement is not sensitive to the spectrum variation but to the phase variation. Hence, this simple whitening process does improve the spectral content and at the same time allows us to postpone the rotation step. Other methods, such as weighting by the mean of the two spectra or their product, produce similar results. This concludes the data preparation prior to cross-correlation.

north–north, north–east, east–east and east–north cross-correlations are calculated between every station-pair for each day-length record. We stack all available daily cross-correlations for each station-pair into one time-series to enhance the SNR. Because all operators are commutative with the rotation operator, the transverse–transverse, transverse–radial, radial–radial and radial–transverse cross-correlations between each station-pair can be calculated by a linear combination of those four components with coefficients related to the interstation azimuth θ and backazimuth ψ angles. These angles are defined by setting the first station as the 'event' location and the second station as the receiver location so that the rotation is:

$$\begin{pmatrix} TT \\ RR \\ TR \\ RT \end{pmatrix} = \begin{pmatrix} -\cos\theta\cos\psi & \cos\theta\sin\psi & -\sin\theta\sin\psi & \sin\theta\cos\psi \\ -\sin\theta\sin\psi & -\sin\theta\cos\psi & -\cos\theta\cos\psi & -\cos\theta\sin\psi \\ -\cos\theta\sin\psi & -\cos\theta\cos\psi & \sin\theta\cos\psi & \sin\theta\sin\psi \\ -\sin\theta\cos\psi & \sin\theta\sin\psi & \cos\theta\sin\psi & -\cos\theta\cos\psi \end{pmatrix} \times \begin{pmatrix} EE \\ EN \\ NN \\ NE \end{pmatrix}. \quad (1)$$

Note that both the radial components and the transverse components at both stations point to the same direction, respectively, under our notation, as shown in Fig. 2. The choice to rotate the north and east components into the transverse and radial components after cross-correlation makes the computation considerably more efficient and space saving. We have compared the results from both cases and no differences are observed.

An example of the resulting cross-correlation between stations 116A and R06C is shown in Fig. 3. Both signals at positive and negative correlation lag times, respectively, are observed, corresponding to waves propagating in opposite directions between the stations. A clear difference in arrival time is observed between the waveforms on the transverse–transverse (T–T) and radial–radial (R–R) cross-correlations. Signal arrival times on the vertical–vertical (Z–Z) cross-correlation and the R–R cross-correlation are similar, and result from the Rayleigh wave. The T–T cross-correlation exhibits the faster Love wave arrival. Although both the Z–Z and R–R cross-correlations contain the same Rayleigh wave signal, the Z–Z cross-correlation generally has a higher SNR. Hence, like others before

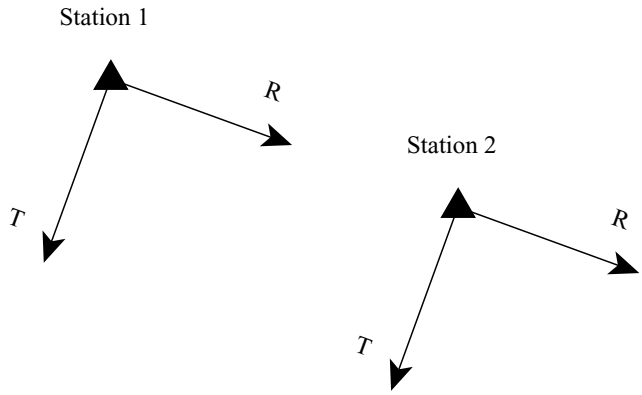

Figure 2. Illustration of how transverse and radial components are defined between two stations.

us, we focus on using Z–Z cross-correlations for the Rayleigh wave analysis.

Theoretical work done by Lobkis & Weaver (2001), Roux *et al.* (2005), Sabra *et al.* (2005b) and Snieder (2004) showed that under a homogenous source distribution assumption, the relationship between the ambient noise cross-correlation $C(t)$ and the estimated Green's function $G(t)$ between stations A and B can be expressed as:

$$\frac{\mathrm{d}C_{AB}(t)}{\mathrm{d}t} = -G_{AB}(t) + G_{BA}(-t) \quad -\infty \le t < \infty. \tag{2}$$

This is equivalent to:

$$G_{AB}(t) = -\frac{\mathrm{d}C_{AB}(t)}{\mathrm{d}t} \quad 0 \le t < \infty. \tag{3}$$

$$G_{BA}(t) = -\frac{\mathrm{d}C_{AB}(-t)}{\mathrm{d}t} \quad 0 \le t < \infty. \tag{4}$$

By the spatial reciprocity of the Green's functions, $G_{AB}(t) = G_{BA}(t)$, we average the positive and negative lag signals to obtain the 'symmetric-signal' of the cross-correlation and then use this symmetric-signal to obtain the final estimated Green's function:

$$G_{AB}(t) = -\frac{\mathrm{d}}{\mathrm{d}t}\left[\frac{C_{AB}(t) + C_{AB}(-t)}{2}\right] \quad 0 \le t < \infty. \tag{5}$$

In most cases, this enhances the SNR and also effectively mixes the signals coming from opposite directions, which helps to reduce the effect of inhomogeneity of the source distribution.

The time-derivative and the sign-flip do not affect the group speed but do alter the signal phase and, hence, the measured phase speed. Without this operation, the symmetric cross-correlation can be thought of as the response due to an impulsive displacement. The traditional definition of the Green's function, however, is the system response to an impulsive force, which is out of phase with displacement by $\pi/2$. In the following, it will be important to remember this phase difference between the cross-correlation and the empirical Green's function. In Bensen *et al.* (2007), the cross-correlation was mistakenly identified with the estimated Green's function. Although both the phase and group velocity analyses based on the Green's function remain correct in that paper, to get unbiased measurements, the cross correlation must first be transformed to the empirical Green's function by using eq. (5) above.

3 EXISTENCE AND STRENGTH OF LOVE WAVES IN AMBIENT NOISE

Figs 4(a) and (b) show record sections centred at the station MOD (Modoc Plateau, CA), for the Rayleigh wave (Z–Z) and the Love wave (T–T), respectively. Signals emerge at both positive and negative correlation lags for Rayleigh and Love waves and Rayleigh waves clearly travel slower than Love waves, as expected. Love

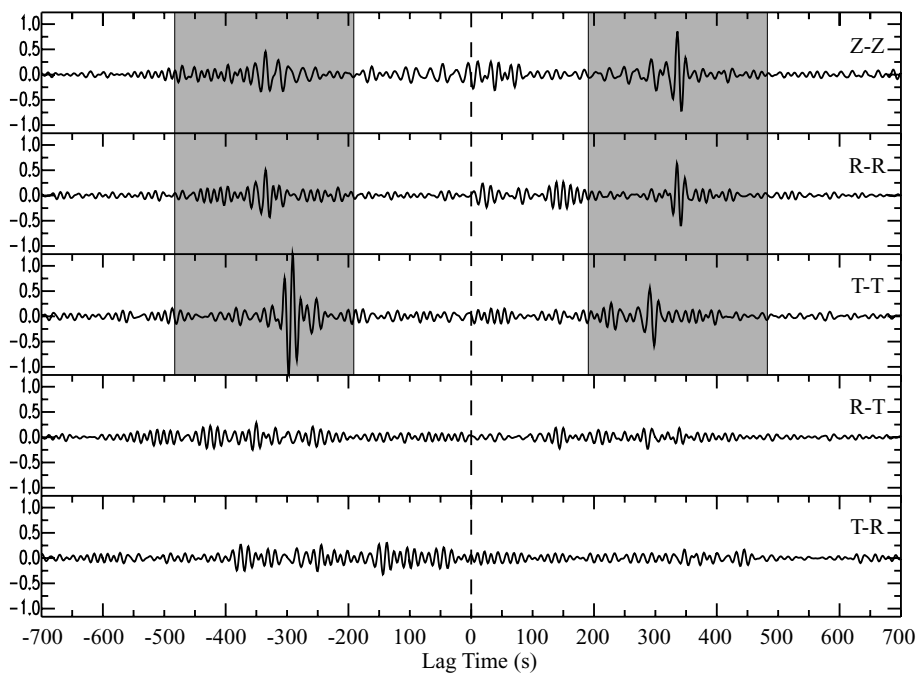

Figure 3. The 10–25 s bandpass filtered cross-correlations observed between two EarthScope/USArray TA stations, 116A (Eloy, Arizona) and R06C (Coleville, California). The prediction windows used for SNR analysis, defined for arrivals with velocities between 2 and 5 km s^{-1}, are marked in grey. Z, R and T denote vertical, radial and transverse, respectively.

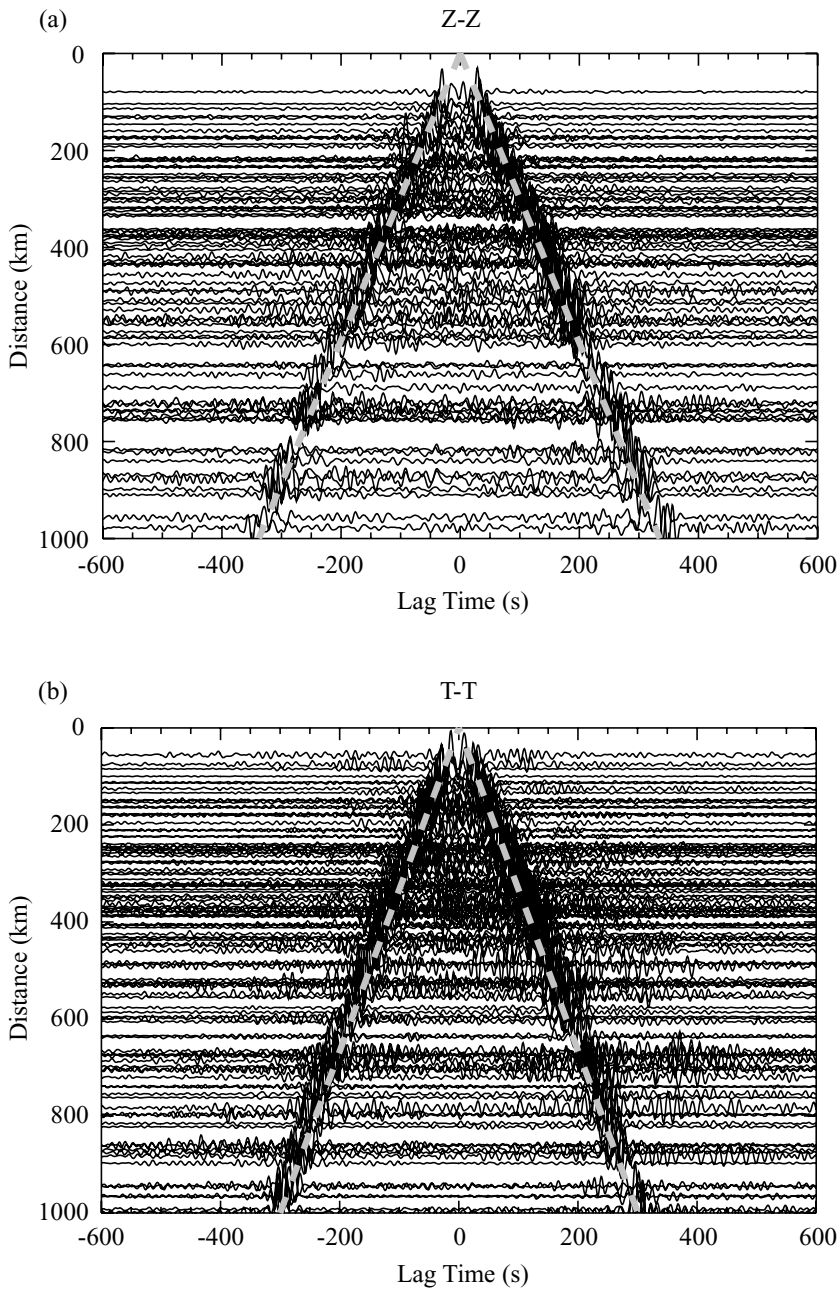

Figure 4. The 10–50 s bandpass filtered cross-correlation record section centred at station MOD (Modoc Plateau, California) with (a) vertical–vertical cross-correlations and (b) transverse–transverse cross-correlations. The dashed lines in (a) and (b) indicate the 3.0 and 3.3 km s^{-1} moveout, respectively. Only the station pairs with SNR higher than 20 at 18 s period are plotted here.

waves, in fact, are commonly observed on cross-correlations across the western United States.

In order to quantify the strength of the signals, for each station-pair we calculate the spectral SNR by computing the ratio of the signal peak in the predicted arrival window to the root mean square (rms) of the noise trailing the arrival window, or 'trailing noise', in each period band for the symmetric component cross-correlation. The prediction window is defined by assuming that the waves travel between 2 and 5 km s^{-1} (Fig. 3), and the noise window starts 500 s after the prediction window and ends at 2700 s lag time. The SNR provides information on the ratio between the coherent noise, the noise from common sources recorded by both stations, and the incoherent noise, the noise from separate and independent sources, in the ambient noise record. The resulting average SNR for all the station pairs with interstation distance larger than three wavelengths is shown in Fig. 5, where a phase speed of 4 km s^{-1} is used to compute the wavelength here and elsewhere.

The most surprising feature observed in Fig. 5 is that Love waves exhibit higher average SNR than Rayleigh waves, especially between about 10 and 20-s period. Because R–R and T–T cross-correlations have very similar background noise or trailing noise, as both of them result from the horizontal components of the seismogram, the Love wave is relatively stronger than the Rayleigh wave on the horizontal components of the ambient noise. Thus, Love waves cannot be generated exclusively by the scattering of Rayleigh waves. Moreover, the SNR of the Rayleigh wave for both the Z–Z and

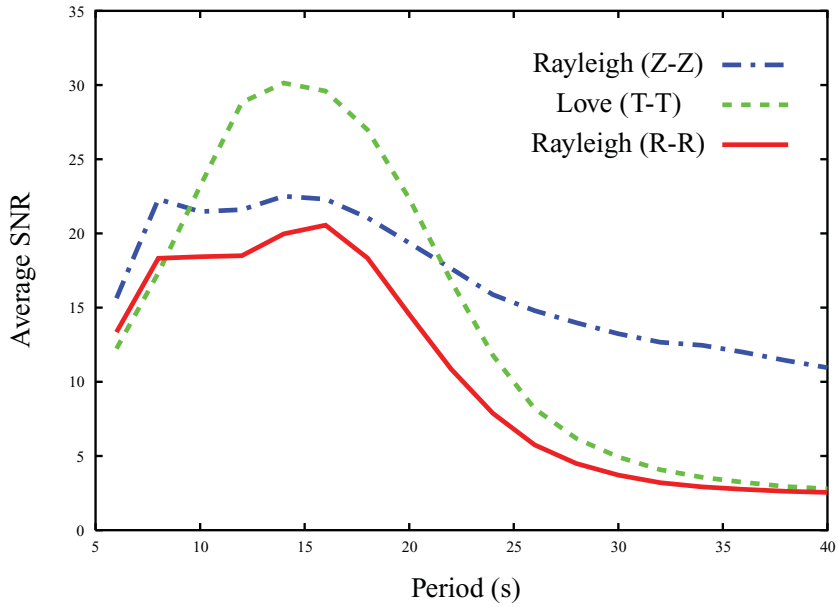

Figure 5. The average SNR for Rayleigh and Love waves. Only station pairs separated by a distance greater than three wavelengths contributed to the average.

R–R cross-correlations exhibits two peaks that correspond to the 8 s (secondary) and 16 s (primary) microseisms, respectively. On the other hand, the Love wave only shows a single peak around a period of 14 s which suggests that the origin of Rayleigh and Love waves may differ in some way.

The SNR drops rapidly for the Love waves above 20-s period, in contrast with the slow drop-off in SNR for the Rayleigh waves on the Z–Z component. However, on the R–R component, the Rayleigh wave SNR remains lower than that of the Love wave up to 40-s period where little signal is detected. This indicates that the horizontal components of the seismograms are heavily contaminated by incoherent local noise, such as tilting by local pressure variations. The drop-off of SNR of Love waves above 20-s period may, therefore, arise from the growth of incoherent local noise rather than the decay of the signal with increasing period. Further investigation of the physical mechanisms as well as the locations of the source of Love wave ambient noise is important to address, but is beyond the scope of this paper.

4 PHASE VELOCITY MEASUREMENT

All data processing described hereafter begins with the estimated Green's functions obtained from the symmetric component of the cross-correlations by applying a negative time-derivative. We used the Z–Z and T–T cross-correlations to obtain the estimated Rayleigh and Love wave Green's functions for each station pair. With the choice of the direction we made on the transverse component (Fig. 2), the Rayleigh and Love wave Green's functions have the same form and the same phase velocity analysis can be applied to both Rayleigh and Love waves.

4.1 Frequency–time analysis

We obtained the Rayleigh wave and Love wave phase velocity dispersion curves by automated frequency–time analysis (FTAN) (Bensen *et al.* 2007). First, FTAN applies a series of Gaussian bandpass filters to the estimated Green's function. The resulting real waveform $f(t)$ at each period can be combined with the imaginary waveform $+iF_H(t)$ to form a complex function $A(t)\ \exp[\ i\varphi(t)]$, where $F_H(t)$ is the Hilbert transform of $f(t)$, $A(t)$ is the envelope function, and $\varphi(t)$ is the phase function. We note that the choice of the positive sign of $+iF_H(t)$ results in a decrease of phase with an increase in time. This choice is somewhat arbitrary; but must be consistent with the theoretical phase as shown in the eq. (6) below. After obtaining the envelope and phase functions, the group traveltime, $t_{\max}$, is measured directly as the peak of the envelope function, and the group velocity is simply $r/t_{\max}$, where r is the distance between the two stations. The corresponding instantaneous frequency at $t_{\max}$ is determined by taking $\omega = [\frac{\partial\varphi(t)}{\partial t}]_{t=t_{\max}}$, which deviates from the centre frequency of the Gaussian bandpass filter slightly. Theoretically, for an instantaneous frequency ω the phase of the estimated Green's function observed at time t can be expressed as:

$$\varphi(t) = kr - \omega t + \frac{\pi}{2} - \frac{\pi}{4} + N \cdot 2\pi + \lambda \qquad N \in \text{Integer}, \lambda \in \text{Re}, \tag{6}$$

where k is the wavenumber, $\pi/2$ is the phase shift from the negative time-derivative, $-\pi/4$ is the phase shift due to the interference of a homogeneous source distribution (discussed further in Section 6.2 below), $N \cdot 2\pi$ is the intrinsic phase ambiguity of phase measurement, and λ is the source phase ambiguity term or 'initial phase' that arises from the uncertainty of the source distribution in addition to other factors.

Note that under the theoretical expectation for the Green's function, which is the displacement response due to a point force impulse, the $\pi/2$ phase shift accounts for the phase shift between the displacement and the force and the $-\pi/4$ phase shift is the asymptotic remnant of the Bessel function under the far-field approximation. Further discussion on how the $-\pi/4$ phase term arises and how λ may depend on the source distribution appears in Section 6.2.

From eq. (6), the phase velocity c when measured on the empirical Green's function is given by

$$c = \frac{\omega}{k} = \frac{r\omega}{\left[\varphi\left(t_{\max}\right) + \omega t_{\max} - \frac{\pi}{4} - N \cdot 2\pi - \lambda\right]} \tag{7}$$

and the phase traveltime is r/c. In eq. (7), N and λ are still unknowns, however. In order to obtain a reliable, unambiguous phase velocity

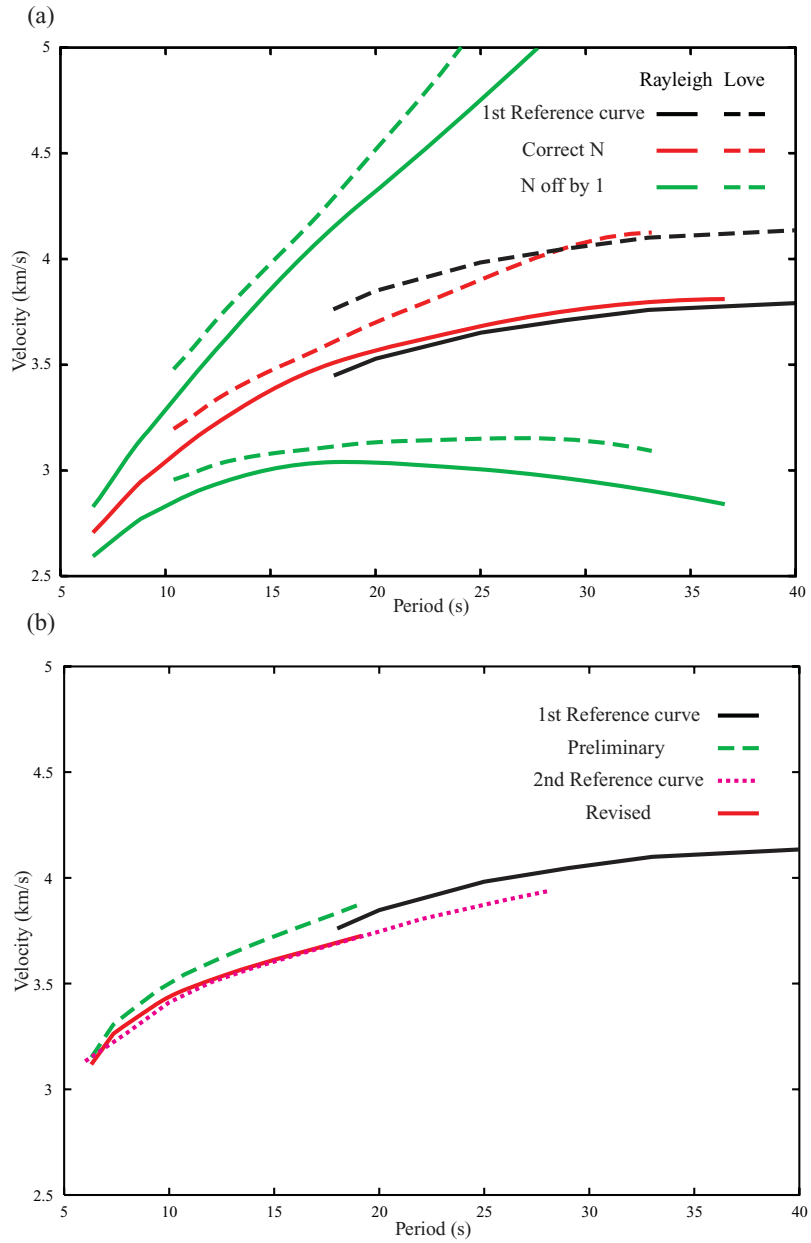

Figure 6. (a) Preliminary phase velocity dispersion curves between stations CVS (Carmenet Vineyards, Sonoma, California) and VES (Vestal, Porterville, California), with various different values of the phase ambiguity factor N in eq. (7). The interstation distance is 409 km. The green lines show the result with the value of N off by ± 1. The red line shows the dispersion measurement obtained by FTAN and the black line is the reference dispersion curve. The Rayleigh wave is shown with solid lines and the Love wave is shown with dash lines. (b) The Love wave dispersion curve between stations A04A and 109C after the first and second measurement. The interstation distance is 1819 km. Both the preliminary and the revised reference curves are shown. The preliminary dispersion measurement is plotted as a dashed green line and the revised dispersion measurement is plotted as a solid red line.

measurement, both N and λ are needed. As we will discuss, N is an integer that can be determined unambiguously in the vast majority of cases. The source phase ambiguity factor λ, however, can be any real number and also can be frequency dependent. It is, therefore, more difficult to constrain, and its determination is the subject of Section 4.2.

We determined N based on a two-step process. First, we compare the resulting measurement with previous phase velocity studies based on earthquake data at long periods ($>$20 s) to obtain the preliminary dispersion curve. Above 20-s period, the surface wave phase velocity variation is relatively small and N off by one can be clearly distinguished when the distance is small ($<$1000 km). Fig. 6(a) shows an example of dispersion curves obtained from cross-correlation of data from stations CVS and VES in California with various different N values and with $\lambda = 0$. Here, we used the average phase velocity curve determined by Yang & Forsyth (2006) in Southern California as the reference curve for the Rayleigh waves. No suitable Love wave reference curve exists, so we increased the Rayleigh wave curve by 9 per cent to give the Love wave reference. By applying a smoothness constraint to the dispersion curves, N at shorter periods ($<$20 s) can also be resolved.

The second step is basically repeating the first step but using a revised reference phase velocity curve between each station pair. To get a more accurate reference curve, we used the preliminary

dispersion measurements obtained using the method described above combined with the selection criteria described in Section 5 to invert for preliminary phase speed maps for periods between 6 and 28 s. We used these maps to estimate the dispersion curves for every station pair which we then used as the reference curves to redetermine N. This second step effectively resolves the 2π ambiguity that cannot be resolved in the first step either due to the lack of good signal at long periods or when the station-pair is at a long distance. Perhaps more importantly, this step makes dispersion measurement a self-consistent process and less dependent on a priori assumptions. More Love wave measurements, but fewer than 4 per cent, were changed after the second step than Rayleigh wave, probably due to the degradation of SNR at long periods. Fig. 6(b) shows an example of Love wave measurement between stations A04A (Legoe Bay, WA) and 109C (Camp Elliot, CA). Due to the extremely long distance (>1800 km) and the lack of good measurement above 20 s, the preliminary measurement had N off by one, but is corrected after the second step. Although this two-steps process effectively allows for identification of the appropriate N for most cases, the same method does not work for λ.

As an example of the resulting Rayleigh and Love wave phase velocity measurements through different geological features, Fig. 7 shows two sets of symmetric component cross-correlations and the resulting phase velocity dispersion curves. The path between O01C (Eel River Conservation Camp, CA) and R04C (Big Horse Ranch, CA) goes through the Sacramento Basin and the path between ORV (Oroville Dam, CA) and TIN (Tinemaha, CA) goes through the Sierra Nevada. A clear velocity contrast at short periods (<15 s) due to the variation of sediment thickness is observed between O01C–R04C and ORV–TIN. The rapid increase of the phase velocity with period for O01C–RO4C between 10 and 20 s is a characteristic feature of thin crust. On the other hand, an almost flat dispersion curve, such as that for ORV–TIN shown here, usually represents a thicker crust. In both cases, the Love wave measurements consistently exhibit higher phase velocities than the Rayleigh wave measurements and approach our preliminary reference models at long periods.

4.2 Three-station method: determination of λ

Theoretical studies have predicted that the 'initial phase', λ, should equal zero under the assumption of a homogeneous source distribution (e.g. Sneider 2004; Roux *et al.* 2005). There is, however, strong observational evidence that the strength of ambient noise is azimuthally heterogeneous (e.g. Shapiro *et al.* 2006; Stehly

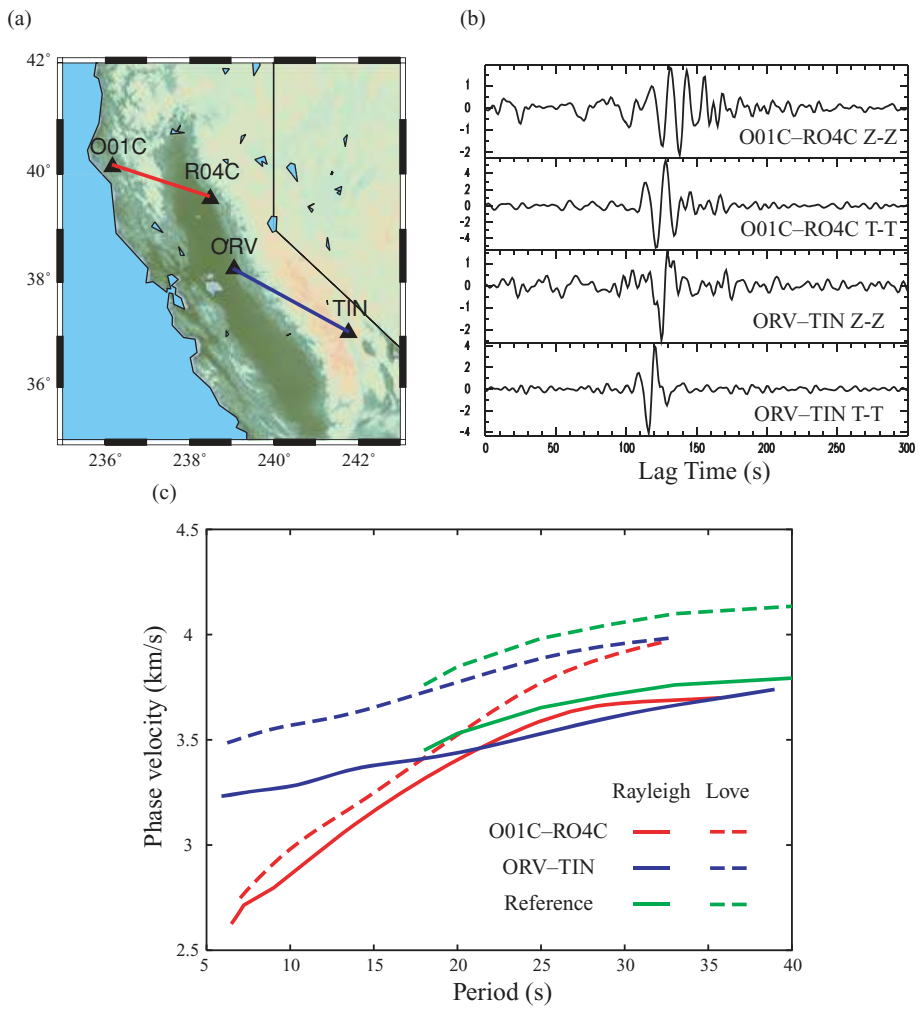

Figure 7. (a) Location of stations O01C, R04C, ORV and TIN. (b) The 5–40 s bandpass filtered symmetric cross-correlations for the vertical–vertical component (Z–Z) and the transverse–transverse component (T–T). (c) The measured Rayleigh and Love wave dispersion curves based on the symmetric cross-correlations shown in (b). The preliminary reference dispersion curves for both Rayleigh and Love wave are shown as green solid and dashed lines, respectively.

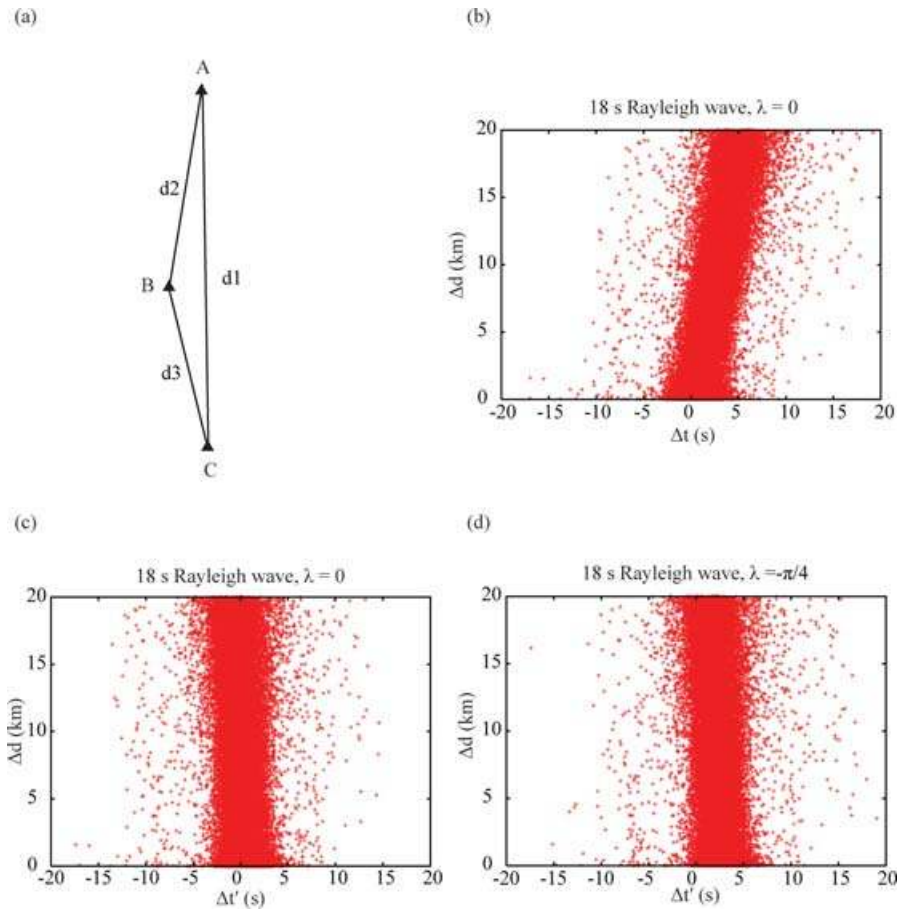

Figure 8. (a) Definition of the interstation distances $d1$, $d2$ and $d3$ used in the three-station analysis of the phase velocity measurements. (b) The relationship observed between distance difference, Δd, and phase traveltime difference, Δt, where the red dots mark individual observations from 40 782 station-triples. (c) The relationship between distance difference, Δd, and the corrected phase traveltime difference, $\Delta t'$, when $\lambda = 0$. (d) Same as (c), but $\lambda = -\pi/4$ is used.

et al. 2006; Yang & Ritzwoller, 2008). It is, therefore, necessary to determine the value of λ empirically. To do this, we compare the phase traveltime (or delay) between station-triples that are nearly aligned along the same great-circle. In general, such station-triples are hard to find, but the TA component of EarthScope/USArray has been laid out approximately on a square grid and many such near station-triples exist. It is the ideal network configuration to resolve this problem.

The idea is as follows. Consider a station-triple that is composed of three nearly colinear stations A, B and C, as shown in Fig. 8(a), where station B lies between stations A and C. Stations A and B are separated by a distance $d2$, B and C are separated by a distance $d3$, and A and C are separated by a distance $d1$. The distance d1 is nearly but not identically equal to the sum of the distances $d2$ and $d3$. If there is no 'initial phase' term for all cases (i.e., if $\lambda = 0$), then the sum of the observed phase times taken on the short-legs, stations A–B and B–C, will approximately equal the phase time observed on the long-leg; that is, between the outside stations A–C, assuming that the wave always propagates in a straight line. Thus, $t1 \approx t2 + t3$. If, however, there is a non-zero 'initial phase' ($\lambda \neq 0$), there will be a difference between the sum of the phase times on the short-legs and that on the long-leg: $t1 \neq t2 + t3$. To interpret each individual deviation is not practical. However, the bulk statistics can be interpreted to produce an estimate of λ. In addition, this three-station method provides information about measurement uncertainties and possible systematic bias.

In performing this analysis, the difference in distance between the sum of the two shorter legs ($d2 + d3$ in Fig. 8a) and the longest leg ($d1$ in Fig. 8a) is limited to less than 20 km. Also, to limit ourselves to reliable velocity measurements but retain a sufficient number of measurements for statistical analysis, the following selection criteria are used. First, the distance between each station-pair in a triple must exceed three wavelengths to satisfy the far-field approximation. Again, a phase velocity of 4 km s^{-1} is used to estimate the wavelength. Second, the SNR at the period of interest must be greater than 17 for all three pairs of stations for the triple to be included in the analysis. We choose these two selection criteria both here and in the tomographic inversion following the analysis done by Bensen *et al.* (2007), which removed most of the erroneous measurements. On top of that, we also limit the distance between each station-pair to no longer than 1000 km to avoid the most serious off-great-circle path and finite frequency effects.

The relationship between distance difference $(d2 + d3) - d1$, or Δd, and phase traveltime difference $(t2 + t3) - t1$, or Δt, at a period of 18 s for all the station-triples that satisfy the above conditions, 40 782 in total, is plotted as an example in Fig. 8(b). A clear trend is seen, with Δt increasing as Δd increases. To account for this slope, a corrected phase traveltime difference $\Delta t'$ is computed as follows

$$\Delta t' = \frac{d1 \cdot (t2 + t3)}{d2 + d3} - t1. \tag{8}$$

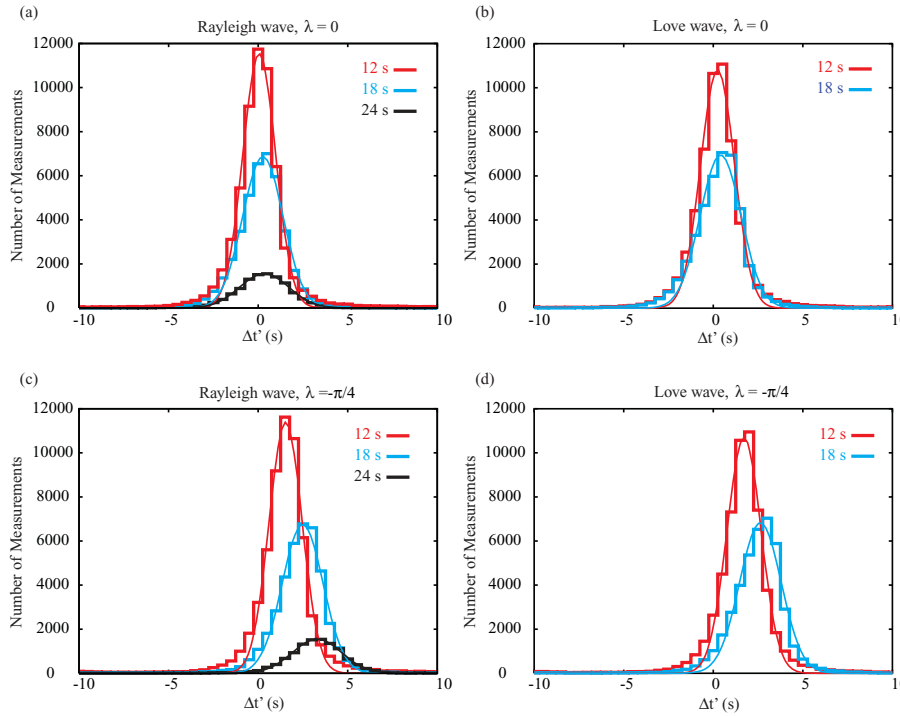

Figure 9. (a) & (b) The histograms of corrected phase traveltime difference, $\Delta t'$, with $\lambda = 0$ for Rayleigh and Love waves. The best-fitting Gaussian curves are also shown. (c) & (d) Same as (a) & (b), but $\lambda = -\pi/4$ is used for comparison.

Table 1. The summary of the three-station analysis.

	Rayleigh wave						Love wave			
	$\lambda = 0$			$\lambda = -\pi/4$			$\lambda = 0$		$\lambda = -\pi/4$	
	12 s	18 s	24 s	12 s	18 s	24 s	12 s	18 s	12 s	18 s
$\overline{\Delta t'}$ (s)	0.056	0.262	0.337	1.535	2.486	3.291	0.237	0.409	1.718	2.631
σ (s)	0.912	1.127	1.372	0.922	1.139	1.381	0.945	1.144	0.952	1.159

Here $\frac{t2+t3}{d2+d3}$ can be considered as the average slowness for the wave travelling through $d2$ and $d3$. The relationship between Δd and $\Delta t'$is plotted in Fig. 8(c), where we have set $\lambda = 0$, and the majority of the measurements aggregate near $\Delta t' = 0$. With the 'initial phase' $\lambda = -\pi/4$, the result is presented in Fig. 8(d) for comparison. In this case, most of the $\Delta t'$ shift by 2.25 s to the right and the majority of the $\Delta t'$ clearly deviate from zero. This deviation indicates a systematic bias in the measurement, in this case caused by the wrong value of λ. Only a few points with $|\Delta t' - \overline{\Delta t'}| > 10$ s are observed in Fig. 8(c), where $\overline{\Delta t'}$ is the mean of $\Delta t'$, indicating that all the N values in eq. (7) are chosen accurately. We have also performed the same analysis after the first step of the dispersion measurement described above. Around 1 per cent of the total points were observed with $|\Delta t' - \overline{\Delta t'}| > 10$ s which resulted from the wrong choice of the N.

Results for the corrected traveltime difference between the long-leg and the sum of the two shorter legs, $\Delta t'$, for the 12, 18 and 24 period Rayleigh waves and the 12 and 18 s Love waves are summarized with histograms in Figs 9(a)–(d). The number of station-triples that pass the selection criteria is too small to be considered statistically significant for the 24 s Love wave. The standard deviation (STDV) and the mean value of the Gaussian fit to these histograms is summarized in Table 1. Results for 'initial phase' $\lambda = 0$ and $-\pi/4$ are used again for comparison. For both Rayleigh and Love waves, with $\lambda = -\pi/4$, the mean of the Gaussian fit clearly deviates from zero and the deviation increases with period. On the other hand, the deviation from zero is small with $\lambda = 0$ for all cases, although it tends to increase with period as well. We believe that $\overline{\Delta t'}$ provides an upper bond on the expected bias in ambient noise measurements caused by an inhomogeneous source distribution, which is between 0.1–0.3 s for Rayleigh waves and 0.2–0.4 s for Love waves.

To further investigate the nature of these small deviations when $\lambda = 0$ is used, we have tried the same analysis with different selection criteria. We find that the critical controlling parameter for these small deviations is the maximum distance allowed. The smaller the distance allowed, the smaller the deviations are. This is not surprising if we accept the fact that the straight ray approximation becomes less robust when the path becomes longer and the principle of least time will always guarantee the phase traveltime of the longest path to be smaller than the sum of the phase traveltimes of the two shorter paths. Including off-great-circle and finite-frequency effects is beyond of the scope of this study, but we can conclude that by using $\lambda = 0$ the systematic bias due to the inhomogeneous source distribution of the ambient noise is negligible.

We can also estimate the average uncertainty of the measurements from Table 1. If we assume that the three phase traveltimes $t1$, $t2$ and $t3$ are independent measurements, the average uncertainty of each individual traveltime measurement can then be estimated by $\frac{1}{\sqrt{3}}\sigma$, where σ is the STDV in the Gaussian fit. The average phase time uncertainty increases with increasing period as expected, but is

less than 1 s for all cases. An uncertainty of less than half a second would be difficult to attain because 1 sample per second time-series are used in this study. This estimation of the phase traveltime uncertainty is independent of the repeatability of the measurements at different times, which has been performed in other studies (e.g. Bensen *et al.* 2007; Yang *et al.* 2007), and provides a new way to estimate the average traveltime uncertainty. This uncertainty, however, is characteristic of the interstation spacings used in this study, and would be expected to grow with increasing interstation distance.

The three-station method developed here confirms that $\lambda = 0$ is a good approximation for the majority of the measurements and bias caused by an inhomogeneous source distribution is minimal. The results also provide insight into the quality of the phase velocity measurements. Overall, the phase traveltime measurements in this study display a negligible systematic error and an average uncertainty of less than 1 s for periods shorter than 24 s. The implication of these results for the distribution of ambient noise sources is discussed in Section 6.2.

5 PHASE VELOCITY TOMOGRAPHY FOR RAYLEIGH AND LOVE WAVES

The selection of the most reliable measurements for tomography is based on three criteria. First, the distance between two stations must be longer than three wavelengths to satisfy the far-field approximation. Again, 4 km s^{-1} is used as a rule-of-thumb to estimate the wavelength. This introduces an effective long-period cut-off of $r/12$ (in seconds) between stations separated by distance r in km. For example, stations separated by 120 km will not return measurements at periods greater than 10 s. Second, the SNR must be higher than 17 at the period of interest. These two criteria are chosen following Bensen *et al.* (2007). Third, each measurement must be coherent with other measurements as measured by its ability to be fit by a smooth tomographic map.

Fig. 10 shows the number of measurements satisfying the first two selection criteria out of the 31, 878 station-pairs for both Rayleigh and Love waves at different periods. The shapes of the curves are very similar to the average SNR curves shown in Fig. 5. At periods above 20 s, both the R–R Rayleigh and T–T Love wave signals presumably have been obscured by high local noise levels on the horizontal component of the seismogram. This limits the longest period of Love wave tomography in this study to about 20 s. The lower local noise on the vertical component allows us to extend the tomography for Rayleigh waves to significantly longer periods.

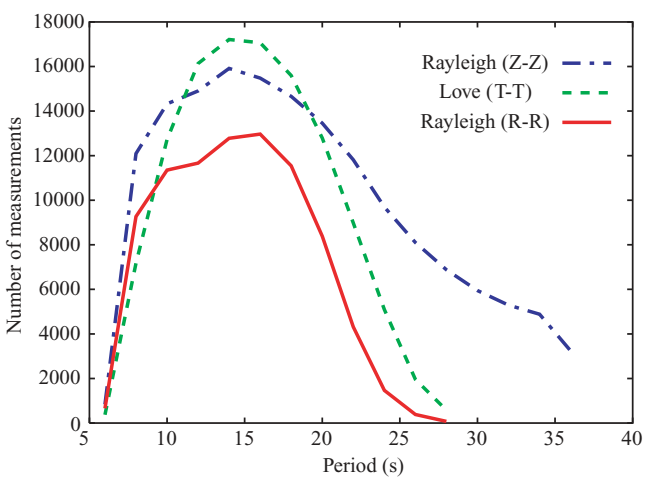

Figure 10. The number of phase velocity measurements satisfying the far-field approximation and the high SNR criterion are presented as a function of period and compared.

We inverted the phase velocity measurements for both Rayleigh and Love waves at 8, 12, 16 and 20 s period for phase speed maps using the tomographic method described by Barmin *et al.* (2001). The method estimates isotropic wave speed by minimizing a penalty function composed of data misfit, model smoothness, and the perturbation $\mathbf{m}$ to an input reference model, $\mathbf{m}_o$, weighted by local path density. Here, we used the average of all selected velocity measurements at each period as our reference model $\mathbf{m}_o$. The method effectively employs 'fat rays', similar to the use of Gaussian beams. Although the result of our three-station method indicates the existence of off-great-circle and finite frequency effect, the effect is in general small. Ritzwoller *et al.* (2002) also showed that diffraction tomography with finite frequency sensitivity kernels recovers similar structures to this version of ray theory at periods shorter than 50 s in most continental regions with dense path coverage. We have no reason to believe that more sophisticated finite-frequency kernels would change the results presented here appreciably, particularly in light of uncertainties in the shape of such kernels, the short periods considered here, and the short interstation paths compared to teleseismic path lengths. However, more careful study needs to be done especially when considering the tomographic inversion including the azimuthal anisotropy when the traveltime effects of off-great-circle paths could prove to be important.

Figs 11(a) and (c) show the typical path coverage for Rayleigh and Love waves, respectively, in the inversion. Figs 11(b) and (d) show the resulting resolution maps estimated with the method described by Barmin *et al.* (2001) with modifications presented by Levshin *et al.* (2005). For each point on the map, the resolution surface resulting from the resolution kernel/matrix is fit locally by a 2-D Gaussian function and twice the estimated standard deviation is identified with the estimated resolution. The resolution across most of the western United States is smaller than 70 km, approximately equal to the average interstation spacing, as expected for good data coverage.

A third data selection criterion must be satisfied by the data. Using data satisfying the first two criteria, we invert for a preliminary oversmoothed map at each period. All the measurements with traveltime residuals larger than 6 s were removed from the data set. This process removed around 1.9, 1.2, 0.4 and 0.2 per cent of the data for the Rayeigh waves at 8, 12, 16 and 20 s and 3.8, 3.4, 1.4 and 0.6 per cent for the Love waves, respectively. More measurements were removed at shorter periods, especially for the Love waves, mainly due to the larger velocity variations that result from structural variations at shallow depth.

Examples of the resulting tomography maps are shown in Figs 12 and 13. The tomography maps at 8, 12, 16 and 20 s for both Rayleigh and Love waves are shown. The black contour plotted on each map encloses the region with an estimated resolution less than 100 km. Any features outside this contour should be interpreted with caution.

The misfit of the tomography maps to the data is summarized in Fig. 14. The small standard deviations (STDV) of the misfits indicate good coherence between the measurements, on average. The gradual increase in STDV with decreasing period reflects stronger heterogeneity in the shallower crust. The fit to the data is in general agreement with the uncertainties that result from the three-station analysis in Section 4.2.

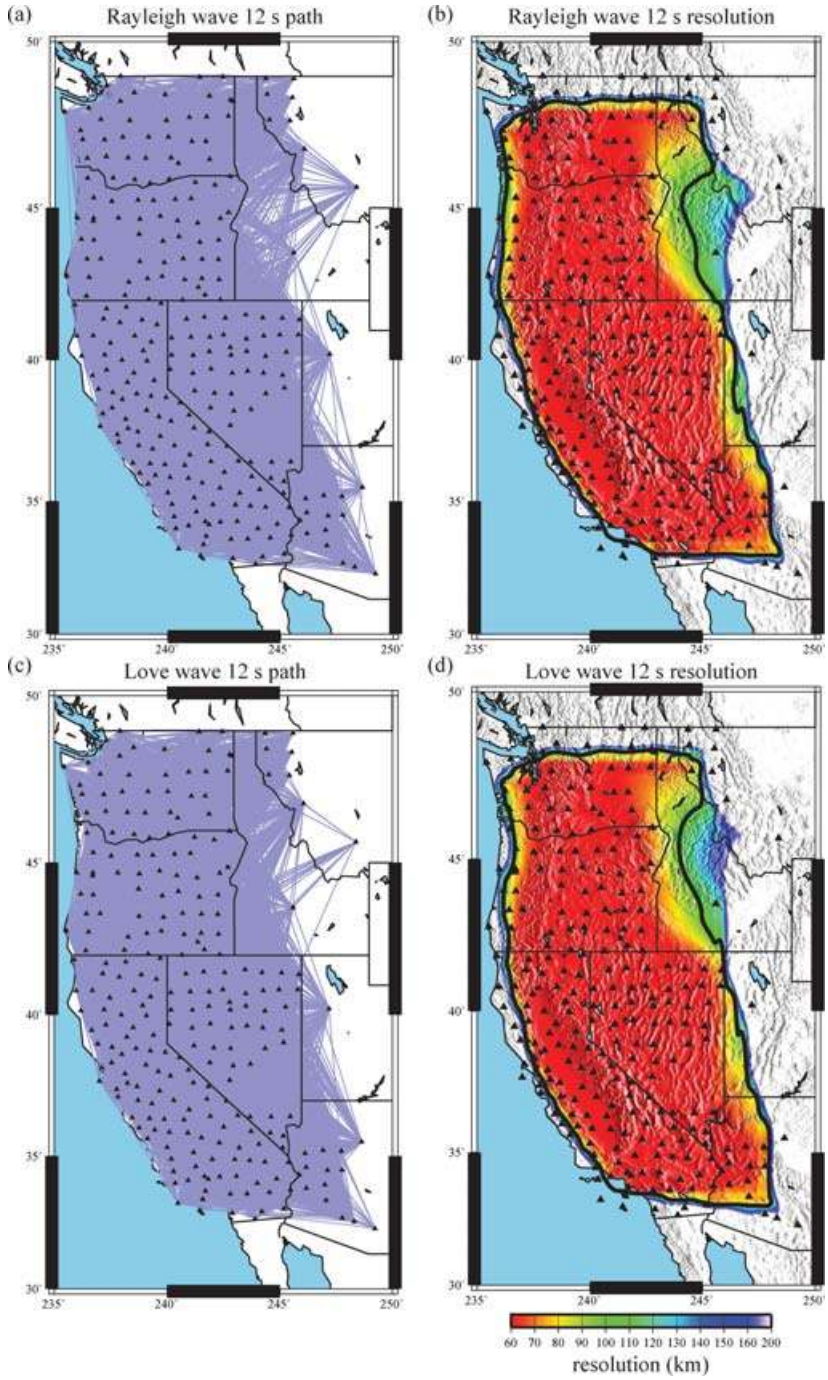

Figure 11. (a) & (c) The ray path coverage by the 12 s Rayleigh and Love wave phase velocity data sets, respectively. (b) & (d) The 12 s resolution maps for Rayleigh and Love waves, respectively, where resolution is defined as twice the standard deviation of a 2-D Gaussian function fit to the resolution matrix at each point. The 100 km resolution contour is shown with a thick black line.

6 DISCUSSION

6.1 Phase velocity maps for Rayleigh and Love waves

As an aid to guide the qualitative interpretation of the phase velocity maps, Fig. 15 displays the radial sensitivity kernels for Rayleigh and Love waves based on PREM in which the ocean is replaced by a sedimentary layer.

The 8 s Love wave map is most sensitive to the upper 10 km of the crust and represents the shallowest structure in all cases. The fast anomaly of the Sierra Nevada and the slow anomaly of the Central Valley of California are the most profound features in the 8 s Love wave map.

The 12 s Love wave and 8 s Rayleigh wave maps are both sensitive to slightly deeper structures and image very similar features, as expected. Again, the fast anomaly of the Sierra Nevada is seen, but the Central Valley anomaly starts to separate into the Sacramento Basin in the north and the San Joaquin Basin in the south. The fast anomaly of the Cascade Range begins to appear from northern California through Washington.

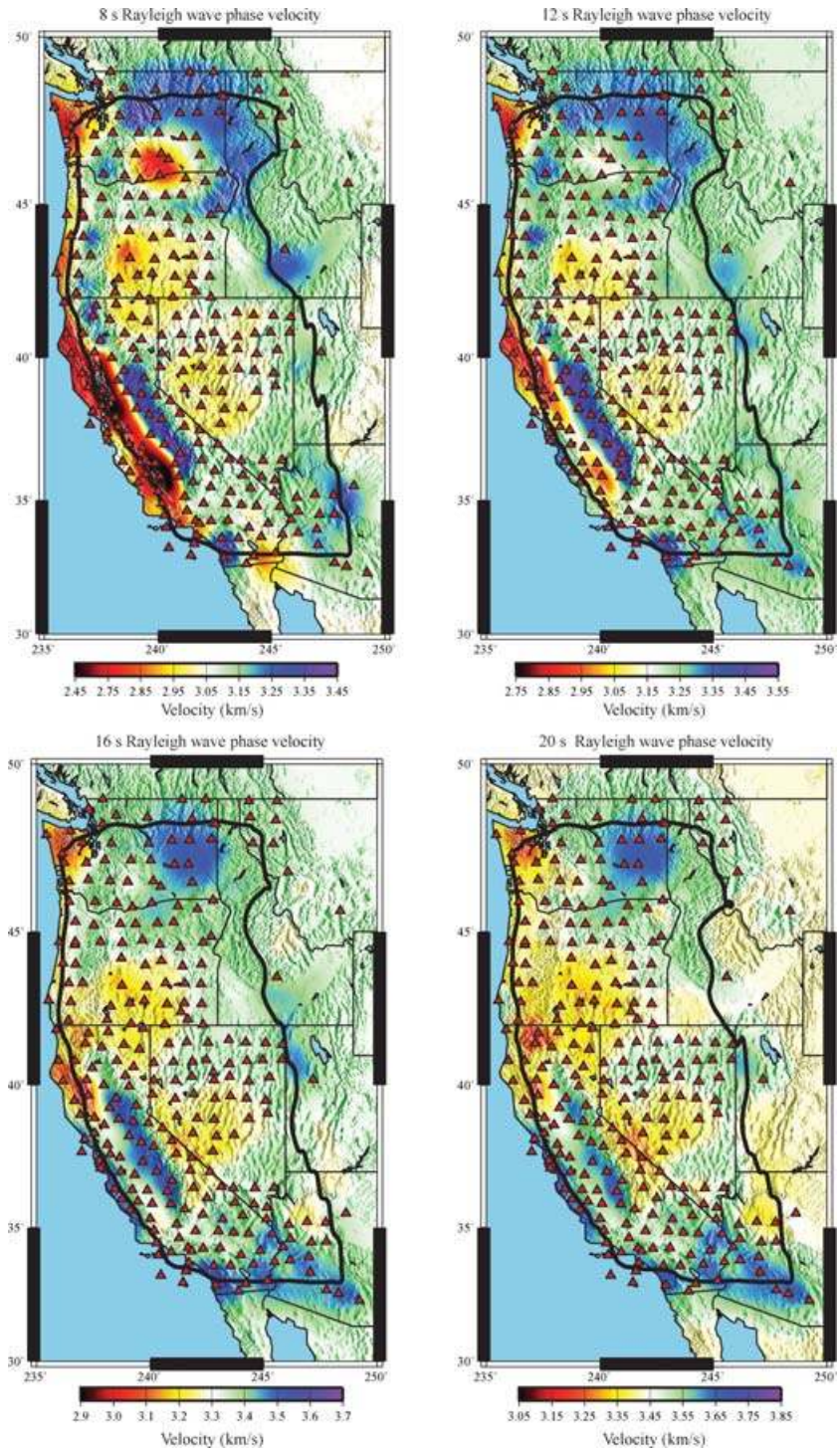

Figure 12. The estimated Rayleigh wave phase velocity maps at periods of 8, 12, 16 and 20 s. The 100 km resolution contour is shown for reference.

The 12 and 16 s Rayleigh wave and 16 and 20 s Love wave maps consistently exhibit similar features. The major slow anomaly of the Central Valley region gradually disappears with increasing period because the surface waves begin to sense the faster shear wave speeds in the crystalline rocks in the underlying basement, and the slow shear wave speeds of the sediment layer are compensated by higher velocities below. In the 20 s Rayleigh wave map, the opposite effect can be seen in the Sierra Nevada region. Due to relatively thick crust, the fast anomaly at shorter periods gradually becomes less prominent at longer periods.

These results are in general agreement with previous studies. Moschetti *et al.* (2007) observed the Rayleigh wave group velocity dispersion in the same region with ambient noise tomography. In general, the phase velocity measurements are sensitive to slightly deeper structures compared to group velocities at the same period. Comparing the 8, 16 and 24 s Rayleigh wave group velocity maps

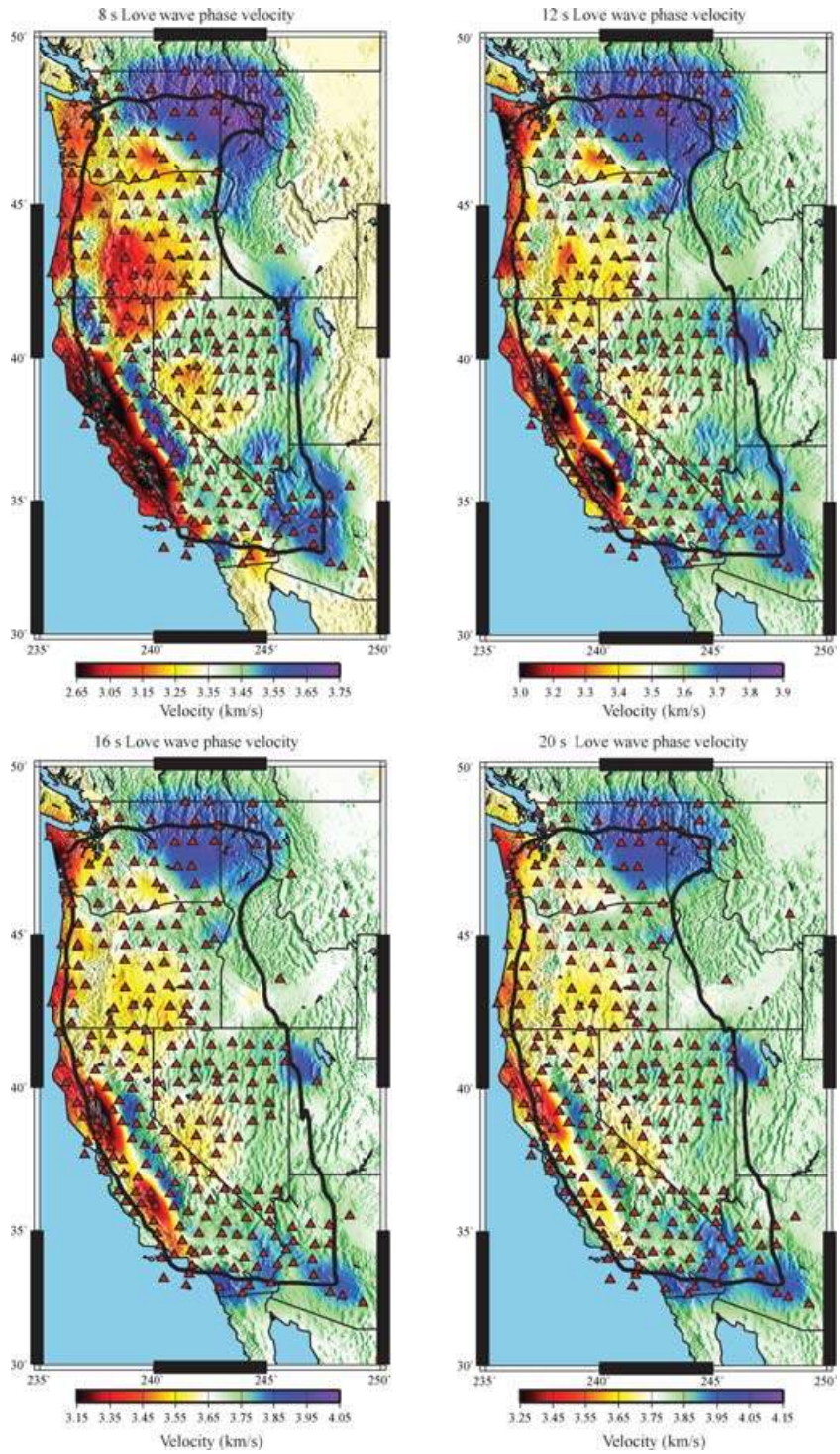

Figure 13. The estimated Love wave phase velocity maps at periods of 8, 12, 16 and 20 s. The 100 km resolution contour is shown for reference.

of Moschetti *et al.* (2007) with our 8, 12 and 20 s Rayleigh wave phase velocity maps, respectively, a striking similarity is observed. Also, there are very similar features on our 25 s Rayleigh wave map (not shown here) with the one reported by Yang & Forsyth (2006) in Southern California, which was constructed using the two plane wave method with teleseismic earthquakes. In Yao *et al.* (2006), a 1.5–3 per cent systematic bias between Rayleigh wave phase velocities between 20 and 30 s period measured by the ambient noise method and the earthquake-based two station method was reported. We compare our mean speed in the Southern California with that obtained by Yang & Forsyth (2006), the difference is less than 0.5 per cent. We suspect the systematic bias observed by Yao *et al.* (2006) is mostly due to bias in the traditional two station method and perhaps too few earthquakes used. In the two station method, the directionality of the incoming teleseismic wave is assumed to be parallel to the great-circle connecting the station and the event. On the other hand, the two plane wave method used by Yang & Forsyth (2006) does not assume this direction for the incoming wave.

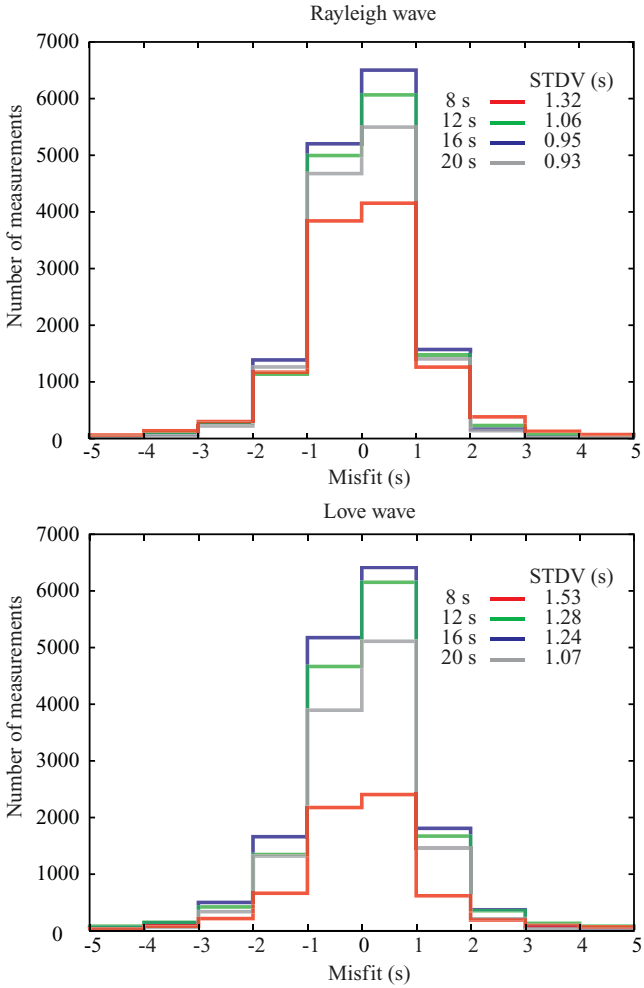

Figure 14. Traveltime misfit histograms for the tomography maps shown in Figs 12 and 13. The standard deviation (STDV) of misfit is also presented.

6.2 Implications for the distribution of ambient noise sources

The source phase ambiguity term or 'initial phase' λ in the eq. (6) was introduced to account for the phase shift due to a possibly azimuthally inhomogeneous distribution of ambient noise sources. We discuss here how source distribution is expected to affect the phase of the cross-correlation and then draw conclusions about the ambient noise source distribution from the three-station method discussed in Section 4.2.

In general, the ambient noise records at two separated stations contain both coherent and incoherent noise. The coherent noise emanates from common sources recorded by both stations. The incoherent noise, on the other hand, results from separated and independent sources. When the cross-correlation is performed, this non-related incoherent noise in the seismograms generates the background noise in the resulting cross-correlation. The signal in the cross-correlation comes from the coherence noise. For a common source cross-correlation, when a homogeneous medium is considered, the 'initial phase' of this cross-correlation at a particular instantaneous frequency is purely determined by the distance difference between the source and the two stations. In consequence, source locations with the same 'initial phase' will lie along hyperbolas with foci at the two stations. Fig. 16 shows an example of the isophase hyperbolas at 50 s period with stations separated by 1000 km, where the 'initial phase' of each neighboring hyperbola differs by π. Over most of the region, the 'initial phase' is sensitive to even slight changes in the azimuth angle, so that when multiple sources are present, destructive interference occurs. The areas with highly stable 'initial phase' occur where the spacing between the adjacent hyperbolas is large. These regions, where sources will interfere constructively, are located on the outward sides of the two stations near the line connecting them. If sources were located exclusively along the outward lines linking the two stations, then uniform constructive interference would occur and instead of the 3-D Green's function, a 2-D Green's function would be obtained. For this case, the $-\pi/4$ that appears in eq. (7) would need to be removed or, alternatively, the 'initial phase' λ would need to be set to $\pi/4$. In contrast, for an azimuthally homogeneous source distribution, the resulting constructive interference in the two outward areas together with the destructive interference for sources elsewhere, results in a $-\pi/4$ phase shift in the cross-correlation relative to if the sources are only located on the outgoing parts of the line connecting the two stations. In this case, a 3-D Green's function is obtained and this phase shift corresponds to the $-\pi/4$ in eq. (7); $\lambda = 0$ in this case. Analytical proof of this phase shift by using the stationary phase approximation can be found in Sneider (2004).

Through our three station analysis, described in Section 4.2 above, we concluded that with $\lambda = 0$ systematic measurement bias is negligible, with an average traveltime uncertainty of about 1 s. This sets an upper bound for the uncertainty of the phase ambiguity λ due to inhomogeneities of the source distribution equal to about $\pi/10$ or one-twentieth of a cycle, because measurement error also contributes to the uncertainty of the measurement. How this small uncertainty of λ fits into the apparently inhomogeneous source distribution around the globe is a non-trivial question. We present here three synthetic experiments based on different source distributions to provide some insight.

In Case 1, synthetic sources are distributed randomly in a 5000 km $\times$ 5000 km square area and the receivers are placed 1000 km apart, as shown in Fig. 16. In this case, with $\lambda = 0$, our measurement procedure is expected to return the input phase velocity. In Case 2, the sources are randomly distributed, but are confined to the line connecting the stations. Instead of $\lambda = 0$, we expect to measure the correct phase velocity only when λ is set equal to $+\pi/4$, which can be derived from eq. (6). In Case 3, the synthetic sources are randomly distributed in the grey area showed in Fig. 16 and we have no priori knowledge of λ. The first two cases here are focused on confirming the method and our idea of 'initial phase', and the third case is what we consider to be a more realistic model of the actual ambient noise source distribution. We choose 3 km s^{-1} as an input phase velocity for a non-dispersive, non-attenuative homogeneous medium. Each synthetic source emits a Gaussian-like wave front with a 3 s width propagating outward with a random initial time and random polarity.

The resulting 5–100 s bandpass cross-correlation functions for all cases are shown in Fig. 17(a). Clear signals are observed on all three cross-correlations. In Case 3, the signals are only observed at positive lag time due to the asymmetry of the source distribution; all sources are to the left of both stations. The signals for all three cases peak at exactly the same lag times due to the constancy of group velocity, but the shape of the signal in Case 2 differs from that in Cases 1 and 3. This is due to the 'initial phase' shift at all frequencies. On the other hand, no clear difference in phase between Cases 1 and 3 is observed. Background noise in the cross-correlation is observed for all cases.

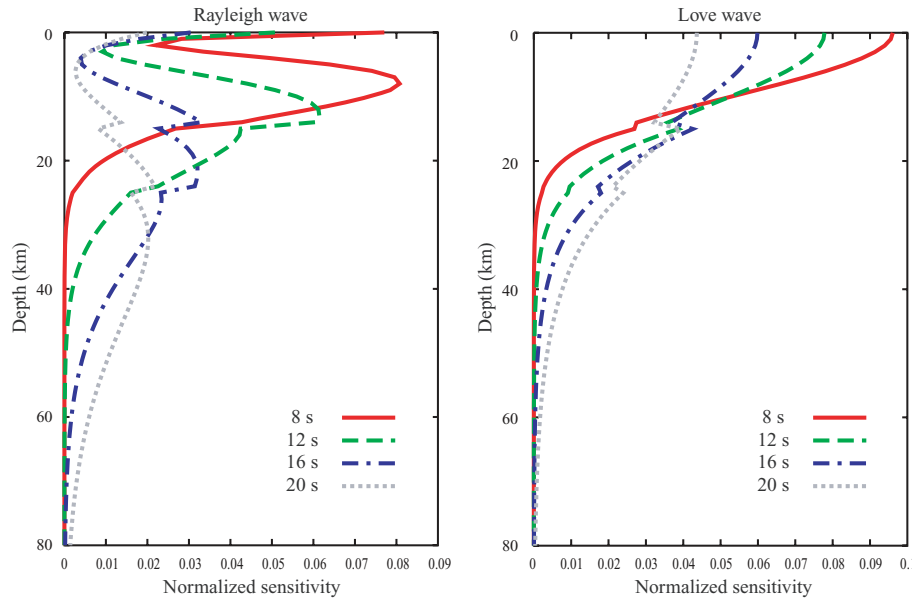

Figure 15. Vertical phase velocity sensitivity kernels of Rayleigh and Love waves at periods of 8, 12, 16 and 20 s, calculated with the 1-D PREM model in which the ocean is replaced by a sedimentary layer.

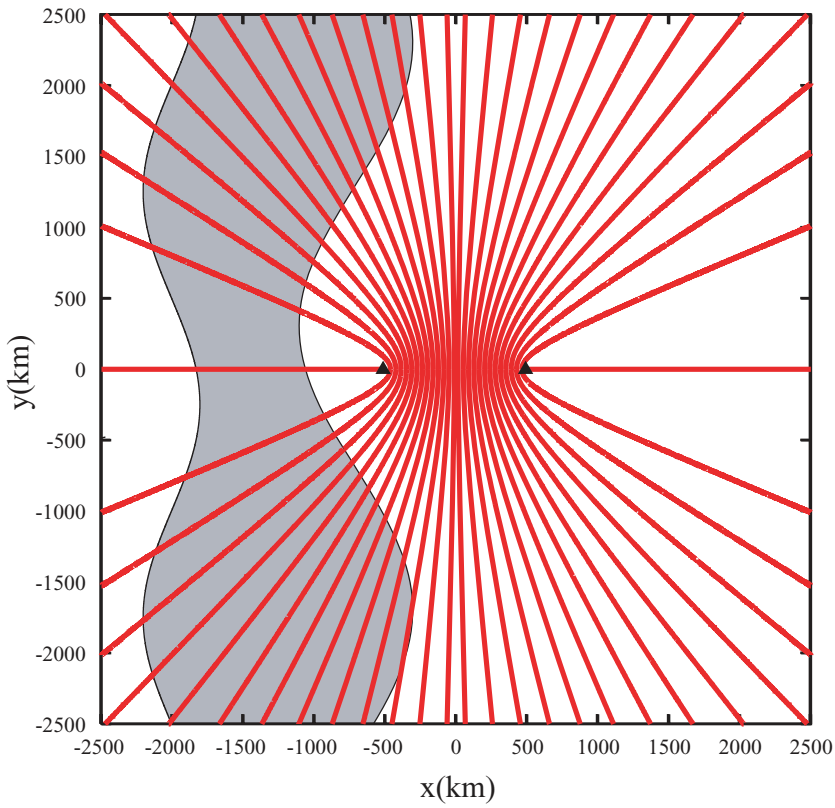

Figure 16. An example of iso-phase hyperbolas each separated from its nearest neighbor by $\pm\pi$. A phase velocity of 3 km s^{-1} for 50 s period is used to construct the hyperbolas. The same setup parameters were used for the synthetic experiments. The grey area defines the region over which sources were randomly distributed for the synthetic experiment referred to as Case 3.

The phase velocity dispersion curves measured by FTAN are shown in Fig. 17(b) for all three cases. The medium is non-dispersive, so the group and phase speeds are the same. The velocity dispersion curves for Cases 1 and 2 confirm our method and the idea of how phase depends on the source distribution. When $\lambda = 0$ and $+\pi/4$ is applied to Cases 1 and 2, respectively, the measured phase velocities match the input phase velocity (3 km s^{-1}) at all periods with errors less than 0.5 per cent. At the same time, similar results are obtained when $\lambda = 0$ is used in Case 3, although the source distribution is highly inhomogeneous. An example of the effect of using

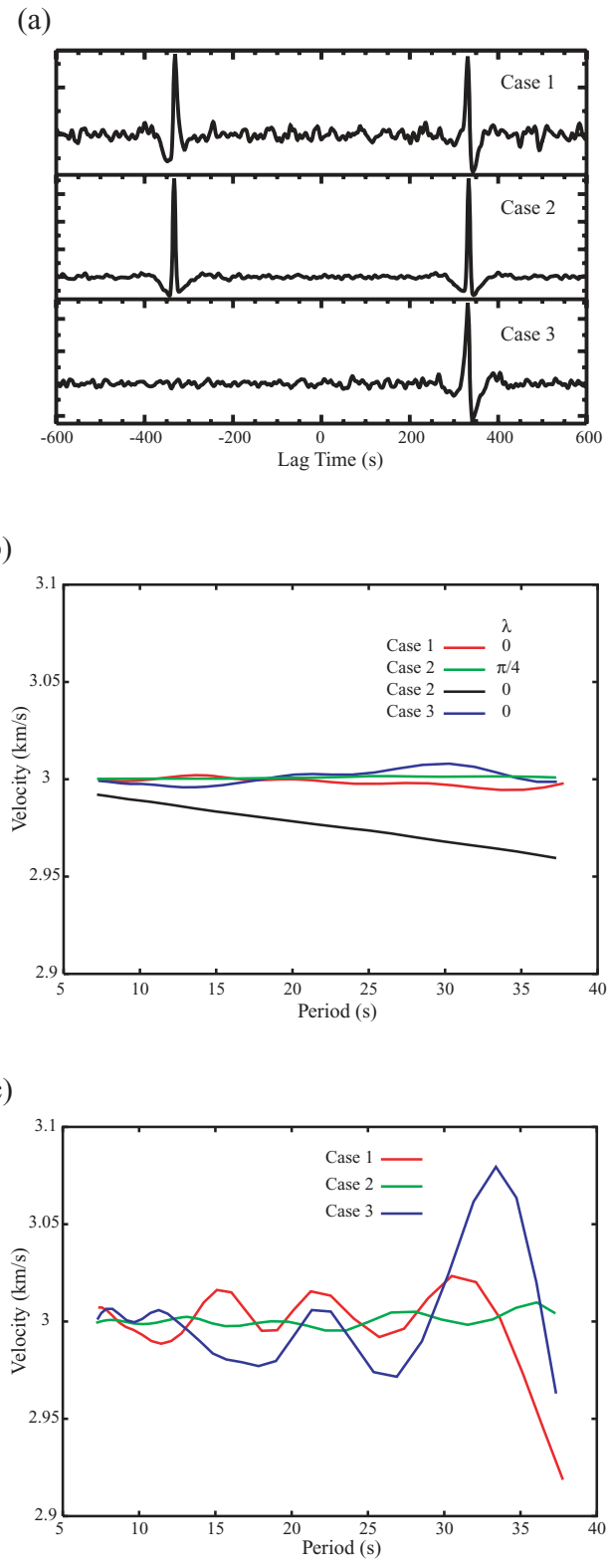

Figure 17. (a) The synthetic cross-correlations recovered for Cases 1, 2 and 3. (b) The phase velocity dispersion curves result from the estimated Green's functions derived from the synthetic cross-correlations in (a). Two 'initial phase' values, 0 and $\pi/4$, are used to obtain the phase velocity dispersion curve for Case 2. Nearly correct phase velocity, 3 km s^{-1}, is returned when the correct 'initial phase' is applied. (c) The measured group velocity dispersion curves for Cases 1, 2 and 3.

the incorrect 'initial phase' is also shown by using $\lambda = 0$ in Case 2. The measured phase velocity dispersion curve clearly deviates from the input value and the error increases with period.

For comparison, the group velocity dispersion curves are also shown here in Fig. 17(c) and exhibit the intrinsic uncertainty difference between these two kinds of measurement. Group velocity clearly exhibits higher uncertainty (up to ~2 per cent) and the uncertainty tends to increase with the period, although non-dispersive signals are particularly hard targets for group velocity measurement. Note that the group velocity measurement is not λ dependent; hence even with incorrect 'initial phase', $\lambda = 0$ for Case 2, the same measurement is returned.

Ambient noise source studies have concluded that the interaction between ocean waves and the shallow seafloor is a major mechanism to create ambient noise. Other than a few special cases, such as the 26 s microseism in the Gulf of Guinea documented by Shapiro *et al.* (2006), there is no evidence that ambient noise is generated exclusively in a highly localized area throughout a long period of time. Several theoretical studies (e.g. Webb 2007; Tanimoto 2007) suggest that ocean depth is a major factor in the strength of coupling between oceanic waves and the seafloor. This results in a source distribution region distributed broadly in shallow off-shore regions of the world's oceans, abstractly similar to what we suggest in Fig. 16. In this case, the strength of the source varies rather smoothly across the constructive interference region on both sides of the station pair and the interference effect is nearly the same as if sources were homogeneously distributed at all azimuths. We believe that this is the setting for most of our measurements, and by setting $\lambda = 0$, the phase velocity is measured with considerable accuracy.

7 CONCLUSION

Continuous three-component ambient noise data obtained between 2005 November 1 and 2006 October 31 recorded by more than 250 stations in the Western United States were used to estimate both Rayleigh and Love wave empirical Green's functions between every station-pair. On the transverse–transverse cross-correlation function, the Love wave signal clearly emerges with an average SNR higher than the Rayleigh wave particularly between 10 and 20 s period. This suggests that Love waves cannot be generated exclusively by the scattering of Rayleigh waves. Above 20 s period, the Love wave SNR drops off quickly, likely due to the increase in incoherent local noise levels on the horizontal components. Further research is needed to determine whether by combining with barometric or other data, the local noise level can be ameliorated and longer period Love wave empirical Green's functions can be obtained from ambient noise.

Phase velocity dispersion between each station-pair was measured by frequency–time analysis with the 'initial phase', λ, in eq. (7) set to 0. The consistency and average uncertainty of the measurements were determined by a novel three-station method. The results show that the empirical Green's functions can be estimated from the negative time derivative of the symmetric component cross-correlation function without major bias and with the average uncertainty of the traveltime around 1 second for periods shorter than 24 s. The Rayleigh and Love wave phase velocity maps at four periods, 8, 12, 16 and 20 s, were constructed and show reasonable qualitative agreement with known geological features and with previous studies. The large velocity variations present in the maps together with systematic errors observed in the three-station analysis suggest that both off-great-circle and finite frequency effects should be considered when a future tomography is performed for azimuthal

anisotropy. Future inversion of these data to produce a 3-D crustal model of the western United States with radial anisotropy is a natural extension of this study.

ACKNOWLEDGMENTS

The data used in this research were obtained from the IRIS Data Management Center and originate predominantly from the Transportable Array component of USArray. The authors are grateful to Toshiro Tanimoto and two anonymous reviewers for comments that helped to improve this paper. This research was supported by a grant from the US National Science Foundation, grant EAR-0450082, and a contract from the US Department of Energy, contract DE-FC52-2005NA2607. MPM acknowledges a National Defense Science and Engineering Graduate Fellowship from the American Society for Engineering Education.

REFERENCES

Barmin, M.P., Ritzwoller, M.H. & Levshin, A.L., 2001. A fast and reliable method for surface wave tomography, *Pure Appl. Geophys.,* **158,** 1351–1375.

Bensen, G.D., Ritzwoller, M.H., Barmin, M.P., Levshin, A.L., Lin, F., Moschetti, M.P., Shapiro, N.M. & Yang, Y., 2007. Processing seismic ambient noise data to obtain reliable broad-band surface wave dispersion measurements, *Geophys. J. Int.,* doi:10.1111/j.1365-246X.2007.03374, **169,** 1239–1260.

Bensen, G.D., Ritzwoller, M.H. & Shapiro, N.M., 2008. Broad-band ambient noise surface wave tomography across the United States, *J. geophys. Res.,* doi:10.1029/2007JB005248, in press.

Campillo, M. & Paul, A., 2003. Long-range correlations in the diffuse seismic coda, *Science,* **299,** 547–549.

Kang, T.S. & Shin, J.S., 2006. Surface-wave tomography from ambient seismic noise of accelerograph networks in southern Korea, *Geophys. Res. Lett.,* **33,** L17303.

Levshin, A.L., Barmin, M.P., Ritzwoller, M.H. & Trampert, J., 2005. Minor-arc and major-arc global surface wave diffraction tomography, *Phys. Earth Planet. Int.,* **149,** 205–223.

Lin, F.C, Ritzwoller, M.H., Townend, J., Savage, M. & Bannister, S., 2007, Ambient noise Rayleigh wave tomography of New Zealand, *Geophys. J. Int.,* **72**(2), 649–666. doi:10.1111/j.1365-246X.2007.03414.x, 2007.

Lobkis, O.I. & Weaver, R.L., 2001. On the emergence of the Green's function in the correlations of a diffuse field, *J. Acoust. Soc. Am.,* **110,** 3011–3017.

Moschetti, M.P., Ritzwoller, M.H. & Shapiro, N.M., 2007. Surface wave tomography of the western United States from ambient seismic noise: Rayleigh wave group velocity maps, *Geochem., Geophys., Geosys.,* **8,** Q08010, doi:10.1029/2007GC001655.

Paul, A.,Campillo, M., Margerin, L., Larose, E. & Derode, A., 2005. Empirical synthesis of time-asymmetrical Green functions from the correlation of coda waves, *J. geophys. Res.,* **110,** B08302.

Rhie, J. & Romanowicz, B., 2004. Excitation of Earth's continuous free oscillations by atmosphere-ocean-seafloor coupling, *Nature,* **431,** 552–556.

Rhie, J. & Romanowicz, B., 2006. A study of the relation between ocean storms and the Earth's hum, *Geochem., Geophys., Geosys.,* **7,** Q10004.

Ritzwoller, M.H., Shapiro, N.M., Barmin, M.P. & Levshin, A.L., 2002. Global surface wave diffraction tomography, *J. geophys. Res.,* **107,** 2335.

Roux, P., Sabra, K.G., Kuperman, W.A. & Roux, A., 2005. Ambient noise cross correlation in free space: theoretical approach, *J. Acoust. Soc. Am.,* **117,** 79–84.

Sabra, K.G., Gerstoft, P., Roux, P., Kuperman, W.A. & Fehler, M.C., 2005a. Surface wave tomography from microseisms in Southern California, *Geophys. Res. Lett.,* **32,** L14311.

Sabra, K.G., Roux, P. & Kuperman, W.A., 2005b. Emergence rate of the time-domain Green's function from the ambient noise cross-correlation function, *J. Acoust. Soc. Am.,* **118,** 3524–3531.

Shapiro, N.M., Ritzwoller, M.H., Molnar, P. & Levin, V., 2004. Thinning and flow of Tibetan crust constrained by seismic anisotropy, *Science,* **305,** 233–236.

Shapiro, N.M., Campillo, M., Stehly, L. & Ritzwoller, M.H., 2005. High-resolution surface-wave tomography from ambient seismic noise, *Science,* **307,** 1615–1618.

Shapiro, N.M., Ritzwoller, M.H. & Bensen, G.D., 2006. Source location of the 26 sec microseism from cross-correlations of ambient seismic noise, *Geophys. Res. Lett.,* **33,** L18310.

Snieder, R., 2004. Extracting the Green's function from the correlation of coda waves: a derivation based on stationary phase, *Phys. Rev. E,* **69,** 046610.

Stehly, L., Campillo, M. & Shapiro, N.M., 2006. A study of the seismic noise from its long-range correlation properties, *J. geophys. Res.,* **111,** B10306.

Tanimoto, T., 2007. Excitation of normal modes by non-linear interaction of ocean waves, *Geophys. J. Int.,* **168,** 571–582.

Webb, S.C., 2007. The Earth's 'hum' is driven by ocean waves over the continental shelves, *Nature,* **445,** 754–756.

Yang, Y. & Forsyth, D.W., 2006. Rayleigh wave phase velocities, small-scale convection, and azimuthal anisotropy beneath southern California, *J. geophys. Res.,* **111,** B07306.

Yang, Y. & Ritzwoller, M.H., 2008. The characteristics of seismic noise as a source for ambient noise tomography, *Geochem., Geophys., Geosys.,* submitted.

Yang, Y., Ritzwoller, M.H., Levshin, A.L. & Shapiro, N.M., 2007. Ambient noise Rayleigh wave tomography across Europe, *Geophys. J. Int.,* **168,** 259–274.

Yao, H.J., Van Der Hilst, R.D. & de Hoop, M.V., 2006. Surface-wave array tomography in SE Tibet from ambient seismic noise and two-station analysis - I. Phase velocity maps, *Geophys. J. Int.,* **166,** 732–744.